Supporting Information

Necroptosis inhibition counteracts neurodegeneration, memory decline and key hallmarks of aging, promoting brain rejuvenation.

Running title: Necroptosis inhibition prevents brain aging

Keywords: *Necroptosis, aging, rejuvenation, hippocampus, axon pathology, memory, cognition, synaptic transmission.*

Macarena S. Arrázola[1,2], Matías Lira[3], Felipe Véliz-Valverde[1,2], Gabriel Quiroz[2], Somya Iqbal[4,5], Samantha L Eaton[4], Douglas J Lamont[6], Hernán Huerta[1,2], Gonzalo Ureta[7], Sebastián Bernales[7], J César Cárdenas[1,2,8,9], Waldo Cerpa[3], Thomas M. Wishart[4] and Felipe A. Court [1,2,8,*].

[1] Center for Integrative Biology, Faculty of Sciences, Universidad Mayor

[2] Geroscience Center for Brain Health and Metabolism (GERO), Santiago, Chile.

[3] Departamento de Biología Celular y Molecular, Facultad de Ciencias Biológicas, Pontificia Universidad Católica de Chile, Av. Libertador Bernardo O´Higgins 340, Santiago, Chile.

[4] The Roslin Institute, University of Edinburgh, Edinburgh, UK.

[5] Massive Analytic Ltd., IDEA London, 69 Wilson Street, Moorgate, London EC2A 2BB

[6] FingerPrints Proteomics Facility, School of Life Sciences, University of Dundee, Dundee, UK

[7] Fundación Ciencia & Vida, Santiago, Chile.

[8] Buck Institute for Research on Aging, Novato, CA, USA.

[9] Department of Chemistry and Biochemistry, University of California, Santa Barbara, California, USA

* Contact information: felipe.court@umayor.cl

1. SUPPLEMENTARY MATERIAL AND METHODS

1.1. *Mlkl*-KO mice genotyping

Mice were genotyped by standard polymerase chain reaction methods using a primer mix (5'-TAT GAC CAT GGC AAC TCA CG-3', 5'-ACC ATC TCC CCA AAC TGT GA-3' and 5'-TCC TTC CAG CAC CTC GTA AT-3') that distinguished between wild-type (498 bp product) and the recombined Δ-exon 3 (158 bp) Mlkl loci (Murphy et al. 2013).

1.2. Quantification of GSK'872 in brain and plasma

Brain and plasma samples were obtained from aged mice treated for 1h with GSK'872 (10mg/kg i.p.). The bioanalysis of plasma and brain samples was conducted by LC-MS/MS with a QTRAP 4500 triple quadrupole mass spectrometer (Applied Biosystems SCIEX) in the negative ion mode and interfaced with an Ekspert ultraLC 100-XL UHPLC System (Eksigent). Calibration standards (0.003 to 10 µM) and quality controls (0.02, 0.2 and 2.0 µM) were prepared from naïve mouse plasma in parallel with mouse plasma study samples (60 µL) by precipitation with three volumes of ice-cold acetonitrile containing 20 µM of theophylline. The precipitated samples were centrifuged at 6,100 g for 30 min at 4°C. Following centrifugation, an aliquot of each supernatant was transferred to an autosampler vial and diluted with two volumes of aqueous mobile phase (0.2% formic acid in water). Samples were injected onto a reverse phase analytical column (YMC Triart C18; 2.0 x 50 mm; 1.9 µm; YMC CO) and eluted with a gradient of 0.2% formic acid in Acetonitrile. GSK'872 was monitored by a multiple reaction monitoring (MRM) experiment using an Analyst software (v1.6.2, Applied Biosystems SCIEX). Quantitation was conducted using a MultiQuant software (v2.1, Applied Biosystems SCIEX) and the resulting calibration curve was fitted with a linear regression and 1/x weighting. The lower limit of quantitation (LLOQ) was 0.010 µM.

1.3. Immunohistochemistry

Primary antibodies: pMLKL (1:200, phospho S345, Abcam, ab196436), pRIPK3 (1:300, Abcam ab205421), neurofilament pan-axonal cocktail (1:250, SMI312 clone, Biolegend), non-phosphorylated neurofilament (1:250, SMI32 clone, Biolegend), cleaved-caspase-3 (1:300, Abcam ab49822) and Iba1 (1:500, Wako Chemicals, 016-26721). Sections were washed to remove the excess of primary antibody and incubated with the appropriate Alexa-Fluor secondary antibodies for 2 h at 25 °C (1:1000, Thermo Fisher Scientific). The excess of secondary antibody was washed, and the sections were coverslipped with Fluoromount-G antifade mounting medium (EMS, 17984-25) containing DAPI staining for nuclei detection (Thermo Fisher Scientific). The anti-pMLKL antibody purchase from Abcam (ab196436) was KO-validated by comparison of the immunodetected signal in aged WT mice with the *Mlkl*-KO mice in the hippocampus (**Fig S19**). Immunostained sections were scanned in a Leica DMi8 Fluorescence Microscope fully automatized.

1.4. Tunel Assay

Apoptosis was evaluated by using the Click-iT™ TUNEL Alexa Fluor-488 Imaging Assays kit (Invitrogen, Thermo Fisher Scientific, USA) in accordance with the manufacturer's instructions. DNaseI was used as a positive control for DNA fragmentation.

1.5. Histological Analysis

Free-floating sections were processed for immunohistochemistry as previously described (Oñate et al. 2020). Briefly, slices were quenched with 0.3% H_2O_2 for 30 min, blocked with 5% BSA and 0.2% triton X-100 for 2 h and incubated with primary antibody (rabbit anti-pMLKL, 1:200 Abcam) overnight at 4 °C. Then, sections were washed with 0.1 M PBS and incubated with secondary biotinylated antibody (goat anti-rabbit, 1:500 Vector Laboratories) for 2 h at RT. After washing, slices were incubated with avidin–biotin–peroxidase complex (Vector Laboratories) for 1 h at RT followed by 0.1 M PBS washes and developed with 3,3-diaminobenzidine (DAB, Sigma-Aldrich). Finally, sections were co-stained with Nissl (cresyl-violet staining) to detect nuclei and with Eriochrome-C staining for myelinated-axons detection, and finally mounted on glass slides with Entellan medium (Merck).

1.6. Fluoro-Jade C staining

Brain tissue was mounted on positively charged slides and rehydrated on decreasing concentrations of ethanol. After rehydration, the tissue was pre- treated for 10 min in potassium permanganate and then incubated for 10 min in the dark at 25 °C in Fluoro-Jade C and DAPI (Biosensis, TR-100-FJ). The tissue was then washed with water and let dry overnight. The next day the slides were cleared in xylene and coverslipped with DPX-new mounting solution (Merck Millipore).

1.7. Electrophysiology

Electrophysiological recordings were performed as described before (Carvajal et al. 2018). Briefly, transverse slices (400 µm) from the dorsal hippocampus were cut under cold artificial cerebrospinal fluid (ACSF, in mM: 124 NaCl, 2.6 $NaHCO_3$, 10 D-glucose, 2.69 KCl, 1.25 KH_2PO_4, 2.5 $CaCl_2$, 1.3 $MgSO_4$, and 2.60 $NaHPO_4$) using a Vibratome (BSK microslicer DTK-1500E, Ted Pella, Redding, CA, USA) and incubated in ACSF for 1 hour at room temperature. In all experiments, 10 µM PTX was added to suppress inhibitory GABAA transmission. Slices were transferred to an experimental chamber (2 ml), superfused (3 ml/min, at room temperature) with gassed ACSF (using 95% O_2/5% CO_2) and visualized by trans-illumination with a binocular microscope (Amscope, Irvine, CA, USA). To evoke field excitatory post synaptic potentials (fEPSPs), Schaffer collaterals were stimulated with bipolar concentric electrodes (Tungsten, 125 µm OD diameter, Microprobes) connected to an isolation unit (Isoflex, AMPI, Jerusalem, Israel). The stimulation was performed in the *stratum radiatum* within 100–200 µm from the recording site. Recordings were filtered at 2.0–3.0 kHz, sampled at 4.0 kHz using an A/D converter (National Instrument, Austin, TX, USA), and stored with the WinLTP program. The basal excitatory synaptic transmission was measured using an input/output curve protocol with 10 s of interval between stimuli. Data were collected and analyzed offline with pClamp 10 software (Molecular Devices, San Jose, CA, USA). To generate LTP, we used high-frequency stimulation (HFS) protocol, which consisted of 3 trains at 100 Hz of stimuli with an inter-train interval of 10 s. Data were collected and analyzed offline with pClamp 10 software (Molecular Devices, San Jose, CA, USA).

1.8. Golgi-Cox staining

Golgi-Cox impregnation method was used to analyze dendritic spine density in hippocampal slices by using the FD Rapid GolgiStain™ Kit, following manufacturer instructions (FD Neurotechnologies Inc, MD, USA). See detailed protocol in Supporting Information. Briefly, fixed brains by PFA perfusion were immersed in impregnation

solution (Solution A/ B), and store at room temperature for 2 weeks in the dark. After 72 h in precipitation Solution C, brains were quickly frozen with dry ice and immediately sectioned with a cryostat at a thickness of 120 µm. Coronal brain sections were mounted on gelatin-coated slides, stained with solution D/E, dehydrated with sequential rinses of 50%, 75%, 95% and 100% ethanol and finally mounted with Entellan medium (Merck). Dendritic spines were imaged as Z-stacks images with a Nikon Eclipse E200 microscope by using a 100X objective with immersion oil. Image analyses were performed with the Image J software by Z-projection of the stacks (sum stacks) followed by the measurement of dendrite length with the segmented line tool. Dendritic spines were manually counted in the defined dendrite length and plotted as spine number normalized to 10 µm of dendrite. Between 8 and 10 dendrites were imaged and quantified per mouse, considering n=3 mice per experimental group.

1.9. Luminex Assay

Cytokines levels were analyzed by Luminex Mouse Discovery Assay (R&D Systems, MN, USA) using a self-designed panel of 12 selected cytokines (plate code: LXSAMSM-12), based on color-coded beads, pre-coated with analyte-specific capture antibodies that permits simultaneous analysis of the analytes. Table S1 detailed cytokines and chemokines of the panel, bead region, sensitivity, and the main functions. Analysis and detection were performed in a Dual-laser flow-based detection instrument, Luminex 200 analyzer by Proyecto Luminex, Programa de Virología, Redeca, ICBM, Facultad de Medicina, Universidad de Chile.

1.10. Label-free proteomics

S-Trap processing of samples

Samples were processed using S-trap mini protocol (Protifi) (for 310 ug and 110 ug samples) and S-trap micro protocol (for low conc samples) as recommended by the manufacturer with little modification. After, application of the samples on the S-trap mini spin column, trapped proteins were washed 5 times with S-TRAP binding buffer. A double digestion with trypsin (1:40) was carried out first overnight at 37^{o}C in TEAB at a final concentration of 50 mM, and then for another 4 hrs (1:40) in 50mM TEAB. Elution of peptides from S-trap mini spin column was achieved by centrifugation at 1000 x g for 1 min by adding 50 mM TEAB, then 0.2% aqueous formic acid and finally 50% acetonitrile/0.2% formic acid. Resulting tryptic peptides were pooled, dried, and quantified using Pierce Quantitative fluorometric Peptide Assay (Thermo Scientific).

LC-MS methods

1.5 µg peptide was analysed per sample. Samples were injected onto a nanoscale C18 reverse-phase chromatography system (UltiMate 3000 RSLC nano, Thermo Scientific) then electrosprayed into an Q Exactive Plus Mass Spectrometer (Thermo Scientific). For liquid chromatography buffers were as follows: buffer A (0.1% formic acid in Milli-Q water (v/v)) and buffer B (80% acetonitrile and 0.1% formic acid in Milli-Q water (v/v). Sample were loaded at 10 µL/min onto a trap column (100 µm × 2 cm, PepMap nanoViper C18 column, 5 µm, 100 Å, Thermo Scientific) equilibrated in 0.1% trifluoroacetic acid (TFA). The trap column was washed for 5 min at the same flow rate with 0.1% TFA then switched in-line with a µPAC C18 nano-LC column (200 cm, inter-pillar distance- 2.5 µm, pore size- 100-200 Å, PharmaFluidics). The peptides were eluted from the column at a constant

flow rate of 300 nl/min with a linear gradient from 3.8% buffer B to 12.5% buffer B in 22 mins, then from 12.5% buffer B to 41.3% buffer B in 95 mins, then from 41.3% buffer B to 61.5% in 23 mins and finally to 100% buffer B in 10 mins. The column was then washed with 100% buffer B for 10 min and re-equilibrated in 1% buffer B for 38 mins. Two blanks were run between each sample to reduce carry-over. The column was kept at a constant temperature of 50^{o}C. The data was acquired using a uPAC-compatible easy spray emitter source operated in positive mode with spray voltage at 2.2 kV, and the ion transfer tube temperature at 275^{o}C. The MS was operated in DIA mode. A scan cycle comprised a full MS scan (m/z range from 345-1155), with RF lens at 60%, AGC target 3E6, orbitrap resolution 70,000, maximum injection time at 200 ms and source fragmentation disabled. The MS survey scan was followed by MS/MS DIA scan events using the following parameters: collision energy mode set to linear with a normalized HCD collision energy set to 25, orbitrap resolution 17500, first fixed mass 200 m/z, AGC target 3E6, maximum injection time 55 ms, isolation windows were variable from 5-66 m/z. The inclusion list (DIA windows) and windows widths are shown in **Table S2**. Data for both MS and MS/MS scans were acquired in profile mode. Mass accuracy was checked before the start of samples analysis.

1.11. Analysis of proteomic data

Data filtering and generation of expression ratios

Raw data files from single-shot label-free experiments were converted into Microsoft Excel workbooks and utilised to generate ratios of protein expression within each animal relative to mean expression of n=4 control animals within each comparison (ie. adult: adult (expression ratio=1), aged: adult, *Mlkl*-KO: aged-WT; aged GSK'872: aged vehicle). Proteins identified by fewer than 2 unique peptides were excluded from subsequent analyses in order to ensure maximum identification confidence (**Figure S9**). Average abundances were calculated for each protein within each condition. As the proteomic analysis is confirmatory of the morphological, functional and behavioral assessments carried out in this study, to retain a as high a coverage of the proteome as possible, averages within group could include proteins with an n of 1 or more absent abundance values. Statistics for grouping consistency have been provided (see Figure S15b). Raw data are available online for further analysis. Following this, relative expression ratios per study (ie. aged vs. adult, *Mlkl*-KO vs. aged WT, and aged GSK'872 vs. aged vehicle) were used for subsequent expression profile clustering analyses. UniProt Accession numbers of proteins identified by 2 or more unique peptides with accompanying expression ratios generated as described above were subjected to expression profile clustering in *BioLayout Express^{3D}*. *BioLayout* utilises a user-determined Pearson correlation and the Markov Clustering Algorithm to cluster input data based on user-determined parameter(s) (Enright 2002; Theocharidis et al. 2009). Pearson correlation was set to 0.97 to cluster datasets into distinct subsets based on similarity in expression profile. Discrete clusters exhibiting biologically relevant expression profiles- ie. opposing directionality between aged versus both MLKL-KO and GSK'872 expression ratios (**Fig S10**) were identified and exported as .txt files containing and identifier column and expression ratios, for subsequent analyses in IPA. See Supporting Information for detailed procedure.

Ingenuity Pathway Analysis (IPA)

The Ingenuity Pathway Analysis (IPA) application (Ingenuity Systems, Silicon Valley, CA) was used to visualise and explore the cellular and molecular pathways that may have been altered as result of genetic (*Mlkl*-KO) or pharmacological (GSK'872) inhibition of necroptosis. Without user-directed manipulation, IPA's statistical predictions and annotations are approximately 90% based off on peer-reviewed publications; the remaining 10% of stored interactions have been identified by other in silico techniques. The analyses were performed only using experimentally reported interactions published in peer-reviewed publications stored within the "hand-curated" and continually updated Ingenuity Knowledge database (Ingenuity Systems, Silicon Valley, CA). For more information on the computational methodology underpinning IPA, please refer to http://www.ingenuity.com/.

Prior to all analyses within IPA, input datasets comprising, as described above, mean expression ratios of n=4 animals per experimental group, were converted to fold-change values, and a ±20% cut-off in expression change respective to control was applied within each respective study. Individual analyses of aged vs. adult, *Mlkl*-KO vs. WT, and GSK'872 vs. vehicle were performed prior to a comparative analysis in order to gain insight into potential biological networks distinguishing "normal" versus "necroptosis-inhibited" aging processes.

For canonical pathway analysis, p-values of canonical pathway scores and subsequent ranking for all analyses performed in this study were derived from a Fisher's Exact Test calculating overlap between molecules in each respective input dataset and number of molecules comprising canonical pathway as defined by the Ingenuity Systems Database. Predicted activation z-scores were calculated by weighing the predicted expression change of target molecules as defined by Ingenuity Knowledge Database against the actual expression change of target molecules reported in input dataset. An activation z-score >2 or <−2 is considered statistically significant (Ingenuity Systems, Silicon Valley, CA). Constituent molecules within pathway were colourized with intensity of colour corresponding to magnitude of change.

For diseases and functions analysis, predicted activation z-scores of associated downstream diseases and functions were calculated by weighing the predicted expression change of target molecules associated with specific "diseases or functions" annotation as defined by Ingenuity Knowledge Database against the actual expression change of target molecules reported in input datasets. An activation z-score >2 or <−2 is considered statistically significant. *P*-values of overlap is derived from a Fisher's exact test were derived from a Fisher's Exact Test calculating overlap between molecules in each respective input dataset and number of molecules comprising the known interactome of each regulator as defined by Ingenuity Systems Database. In graphical format, target molecules present within each proteomic dataset predicted to be activated or inhibited to mediate the associated "diseases or functions" annotation were visualised in relation to their associated predicted regulator and were colourised with intensity of colour corresponding to magnitude of change.

2. SUPPLEMENTARY FIGURES

Fig S1

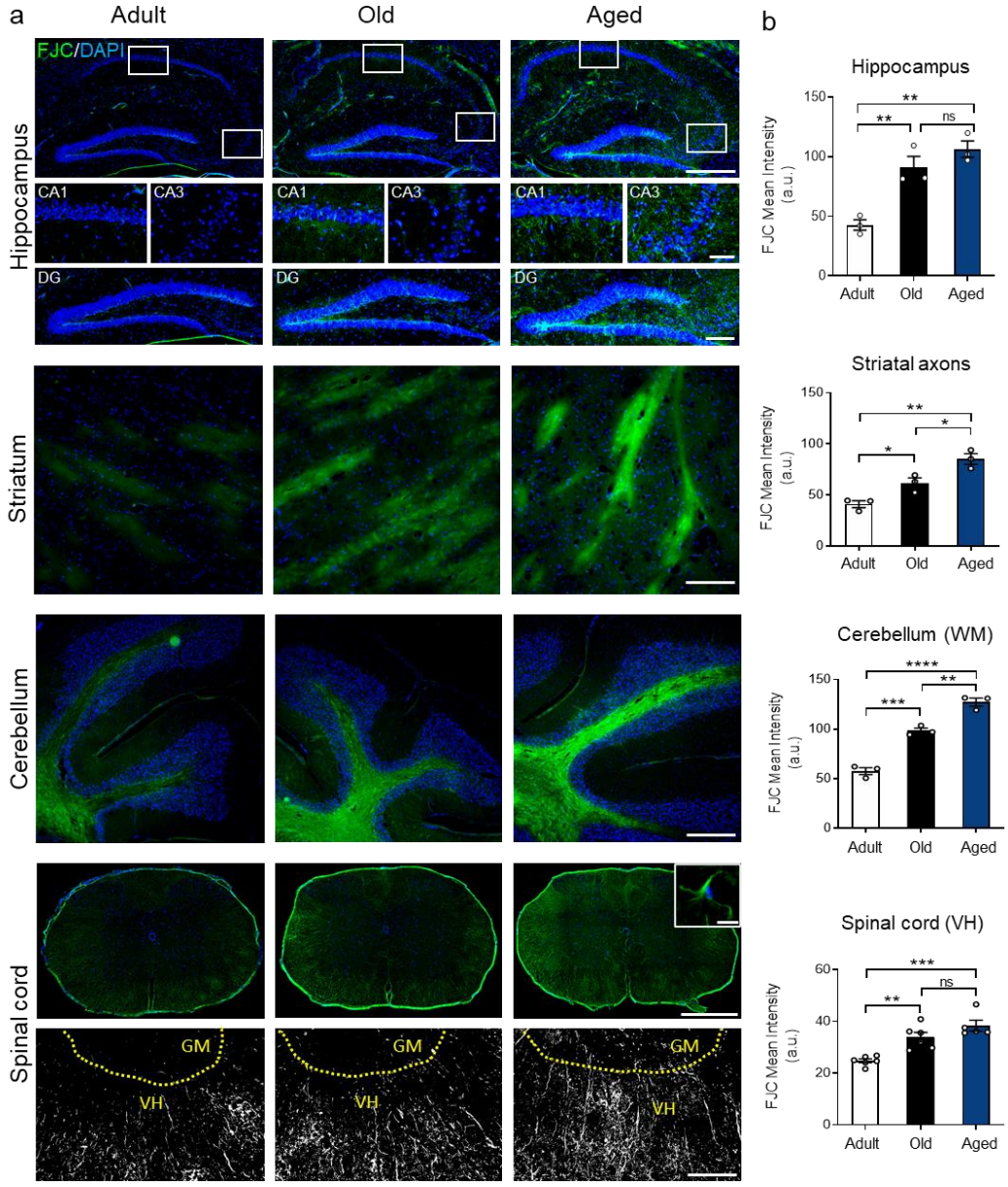

Fig S1. Progression of neurodegeneration in different brain regions along aging. Representative images of Fluoro Jade C (FJC, green) staining in the hippocampus (calibration bar, 500 µm; CA1/3 and DG bars are 100 µm and 200 µm respectively), striatum (calibration bar, 25 µm), cerebellum (calibration bar, 50µm) and spinal cord (calibration bar, 100 µm and 25 µm for the inset) of adult (3-6 month), old (12-15 month) and aged mice (more than 24 month). DAPI staining (blue) detects nuclei **(a)**. Mean intensity of FJC was evaluated in the entire hippocampus, the axonal tracts of the striatum, the cerebellar white matter, and in the ventral (VH) of the spinal cord, GM: gray matter **(b)**. Values are the result of the analysis of n=3-4 mice per group. One-way ANOVA with Tukey analysis for multiple comparisons, *p:<0.05; **p<0.01; ***p<0.005; ****p<0.001.

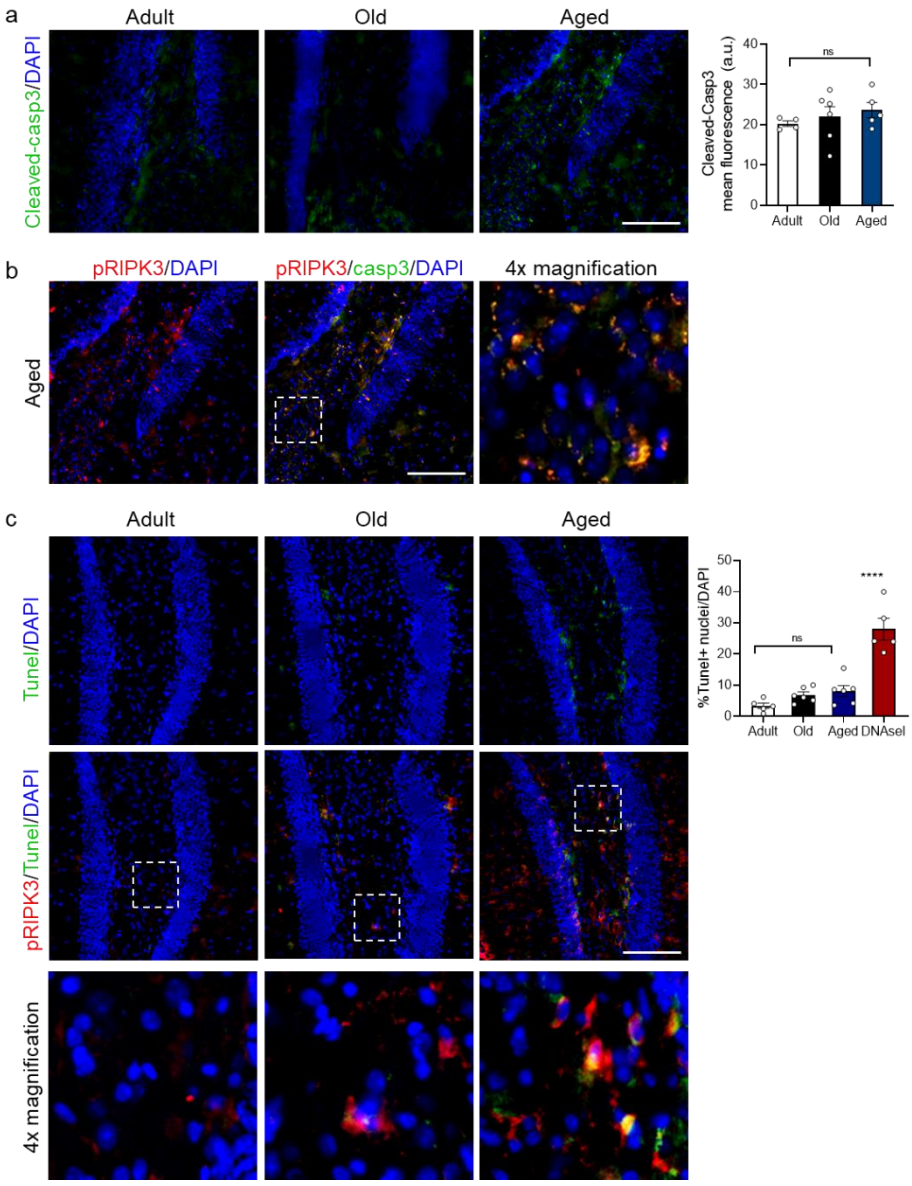

Fig S2. Cell death assessment in the hippocampal DG during aging. (a) Cleaved-caspase-3 levels (green) were measured in the hilus of the DG at different ages, bar: 25 µm. Non-significant differences were observed between groups. One-way ANOVA and Tukey's test for multiple comparison, p=0.519 for adult vs aged, n=5-6 mice. **(b)** Representative image of cleaved-caspase-3 (green) and pRIPK3 (red) co-staining in the DG of aged mice. Bar, 25 µm. Magnification (x4) shows pRIPK3 positive cells co-labeling with activated caspase-3. (c) Fluorescent Tunel assay performed in mouse brain along aging. Images and quantification show an upward trend of Tunel staining (green) along aging, without significant differences (p= 0.345 for adult vs aged, n=5-6). pRIPK3/Tunel co-staining and magnification show increasing levels of pRIPK3 (red) during aging, which overlap with Tunel in the DG of aged mice. One of the values from the adult group was identified as an outlier and was excluded from the analysis. Oultiers were identified with the "Identify Outliers" tool from GraphPad Prism v8.0.2.

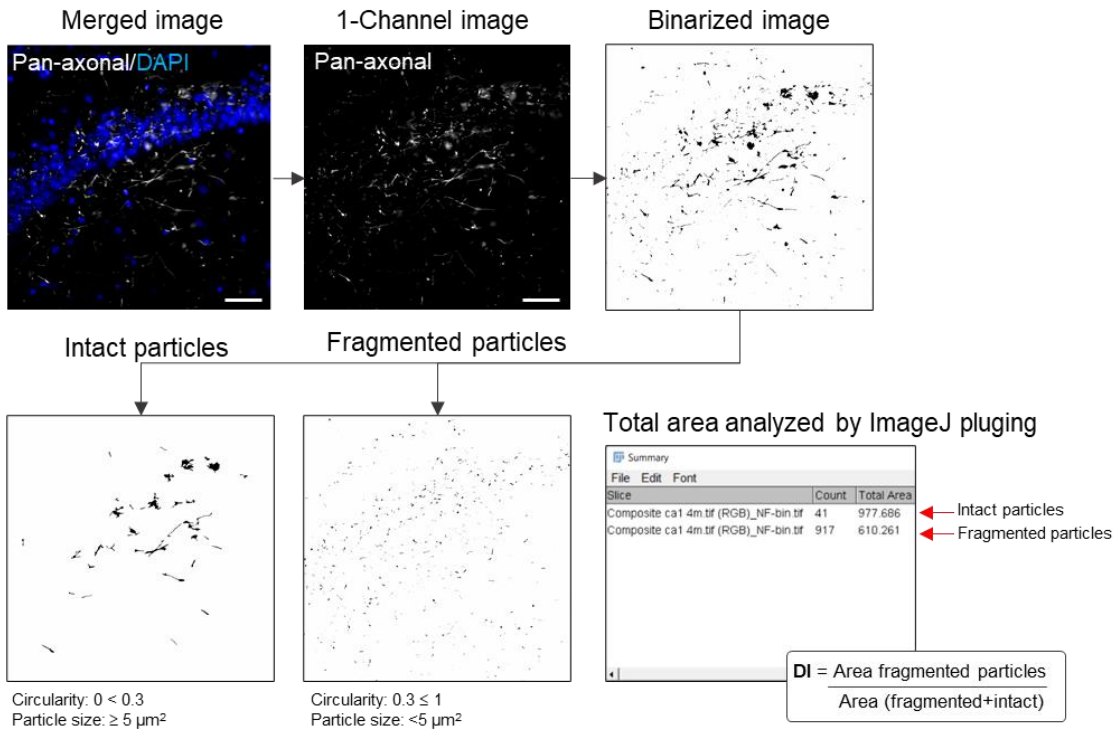

Fig S3. Workflow of Axonal Degeneration Index analysis. Raw images of pan-axonal NF labeling were binarized and subjected to the "Analyze Particles" tool of ImageJ software. Fragmented and intact axonal particles were estimated by defining area and circularity of the particles (fragmented: <5 µm^2 and 0.3 ≤ 1 circularity; intact: ≥ 5 µm^2 and 0<0.3 circularity). Calibration bar, 10 µm. Degeneration Index (DI) was calculated as the ratio between the area of fragmented axons over the total axonal area.

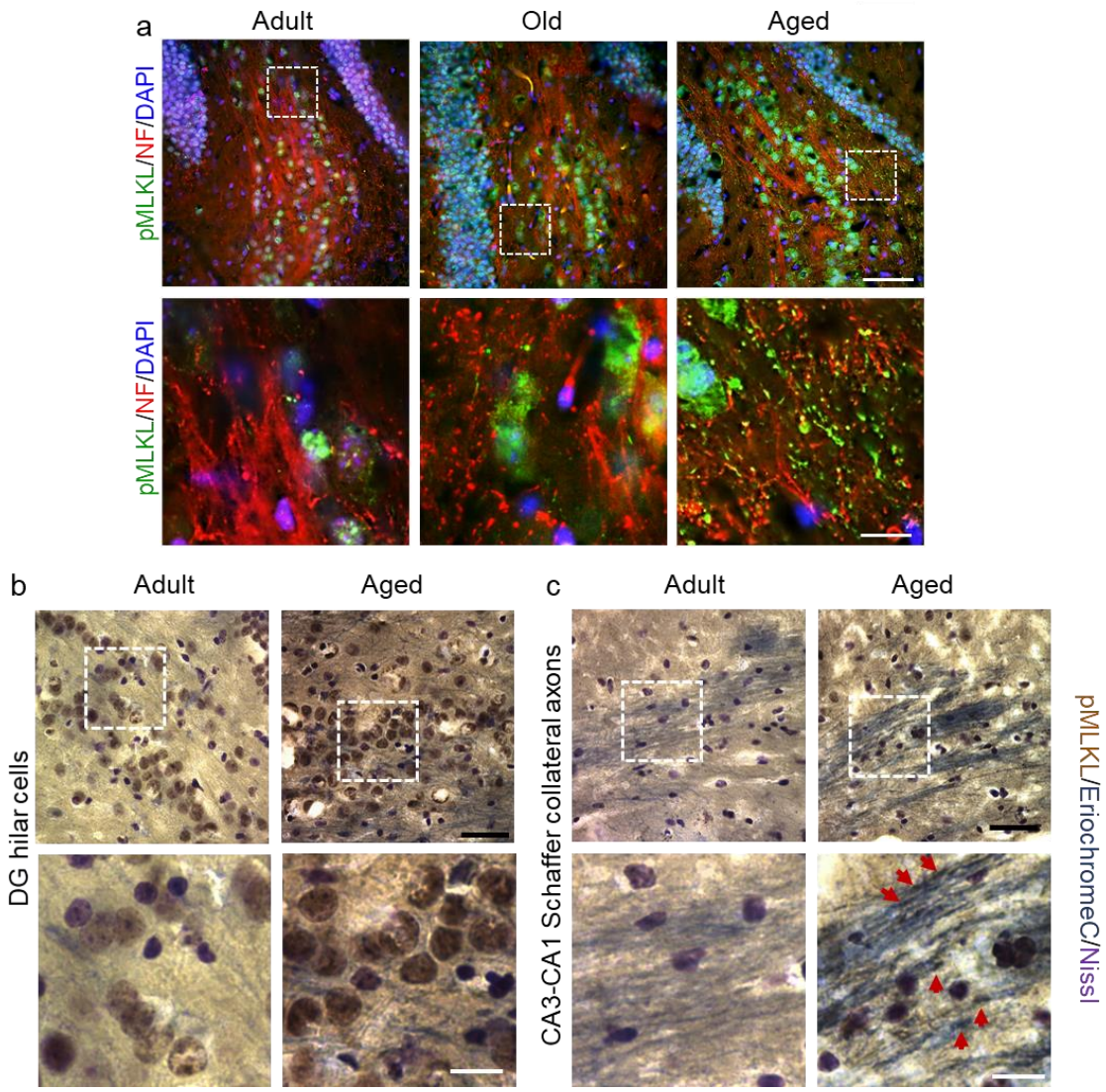

Fig S4. Phosphorylated MLKL detection in hippocampal subareas durong aging. (a) Axonal pMLKL (green) detected in NF-positive axons (red), bar: 25 µm. Dotted boxes correspond to magnified ROIs, bar 5 µm. **(b,c)** Immunohistochemistry against pMLKL (brown) and Eriochrome-C staining (myelinated axons, blue) in the DG and CA3-CA1 axons, respectively; bar: 40 µm. Dotted boxes correspond to image magnification, bar: 15 µm. Increased pMLKL in neuronal somas (dark brown/+Nissl, violet) is observed in the both hippocampal subfields. Aggregation pattern of pMLKL is observed in the Schaffer collateral projections, indicated with red arrowheads.

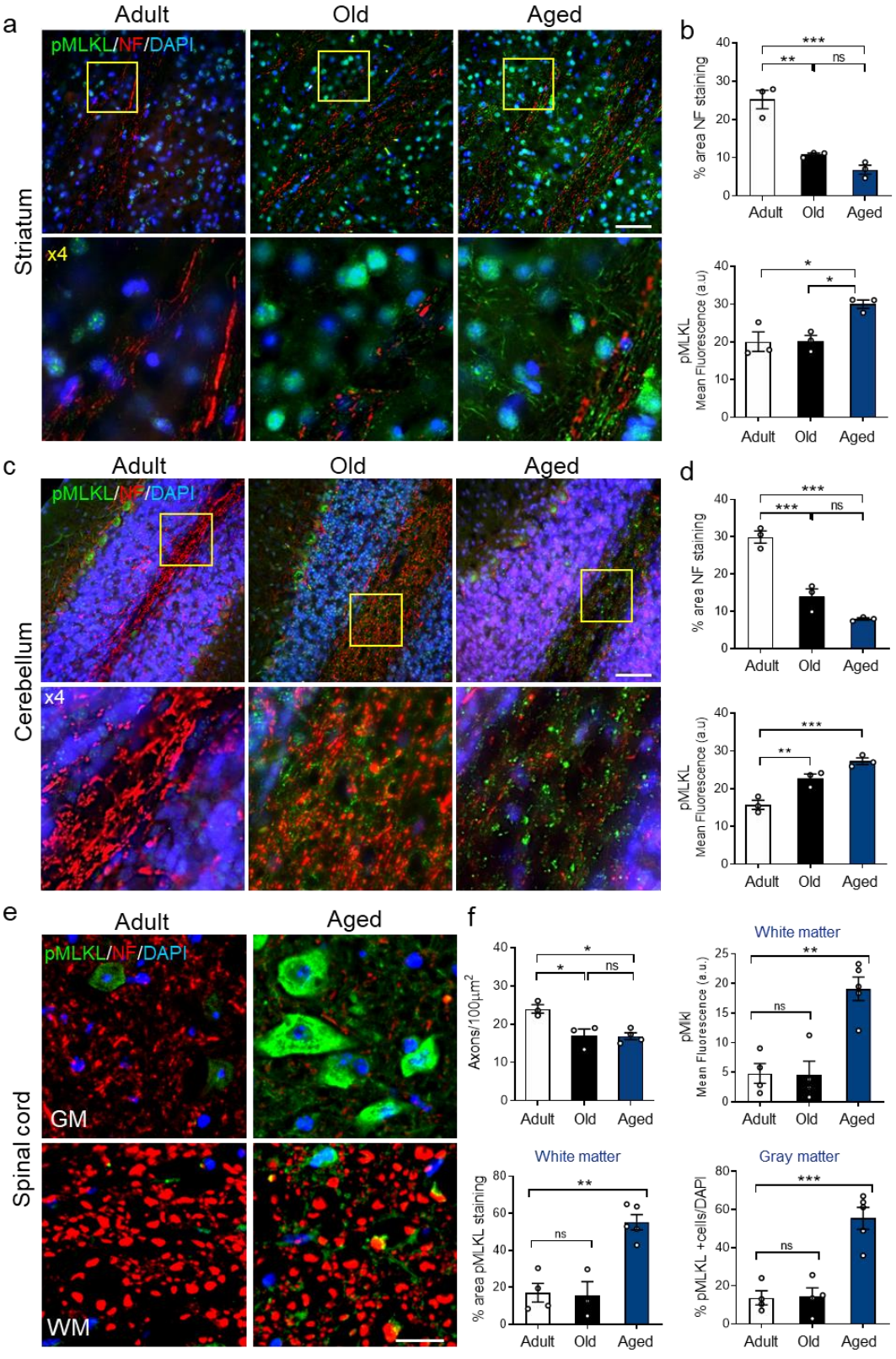
a
Adult
Old
Aged
pMLKL/NF/DAPI
Striatum
x4
b
% area NF staining
pMLKL Mean Fluorescence (a.u)
Adult
Old
Aged
c
Cerebellum
d
e
Spinal cord
GM
WM
f
Axons/100µm²
White matter
Gray matter
% area pMLKL staining
% pMLKL +cells/DAPI
ns

Fig S5. Necroptosis activation is correlated with axonal degeneration in diverse areas of the aging brain. Necroptosis activation was measured through the phosphorylation of MLKL (pMLKL in green) in axon-enriched subfields of different brain areas. Pan-axonal NF antibody (red) was used to stain axons, and DAPI (blue) to detect nuclei and to identify granular cell layers and gray matter regions in the striatum, cerebellum and spinal cord, respectively. **(a,b)** Phosphorylated-MLKL mean intensity increases in axonal tracts of the striatum along aging. Decreased pan-axonal NF staining was used as a readout of axonal degeneration (calibration bar, 25 µm). **(c,d)** Pan-axonal NF staining decreased in the white matter (WM) of the cerebellum, accompanied by an increase in pMLKL staining in the same compartment along aging (calibration bar, 25 µm). **(e,f)** Phosphorylated MLKL levels were evaluated in the white matter (WM) and gray matter (GM) of spinal cord cross-sections during aging. Necroptosis was slightly detected in motor neurons (GM) of adult mice, while no pMLKL signal was observed in the WM (calibration bar, 20 µm). Aged mice present high levels of pMLKL in both, WM and GM measured as pMLKL mean intensity and percentage of stained area. Percentage of pMLKL-positive cells (normalized to DAPI) in the GM also increased in aged mice compare to adult and old groups. Axonal degeneration was assessed by counting the number of axons per area in the WM. Values are the result of the analysis of n=3-6 mice per group. One-way ANOVA with Tukey analysis for multiple comparisons, *p:<0.05; **p<0.01, ***p<0.005.

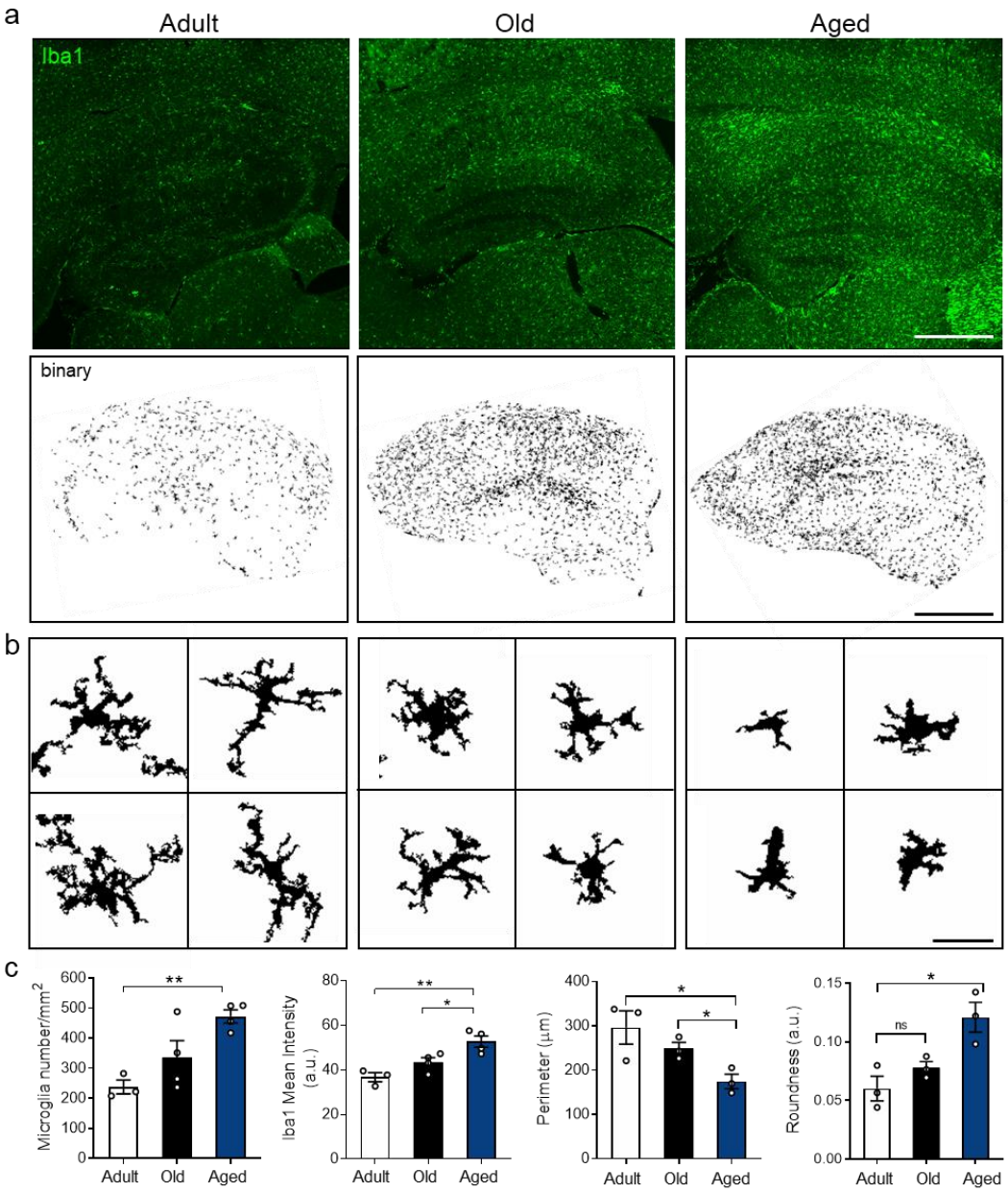

Fig S6. Increased neuroinflammation is correlated with morphological changes associated to pathological microglia activation in aging. (a) Microglia number and intensity were evaluated by Iba1 immunostaining (green), (calibration bar, 200 µm). **(b)** Morphological classification of microglia was performed from Iba1-stained and binarized images. (Adult: resting microglia; Old: primed microglia; Aged: pathologic activation, calibration bar, 30 µm). **(c)** Increased number of microglia and Iba1 intensity were observed in the hippocampus of aged mice. Morphological parameters of microglia reshaping during activation were also evaluated, including decreased perimeter and cell roundness. Values are the result of the analysis of n=3-8 mice per group. One-way ANOVA with Tukey analysis for multiple comparisons, *p:<0.05. **p<0.01.

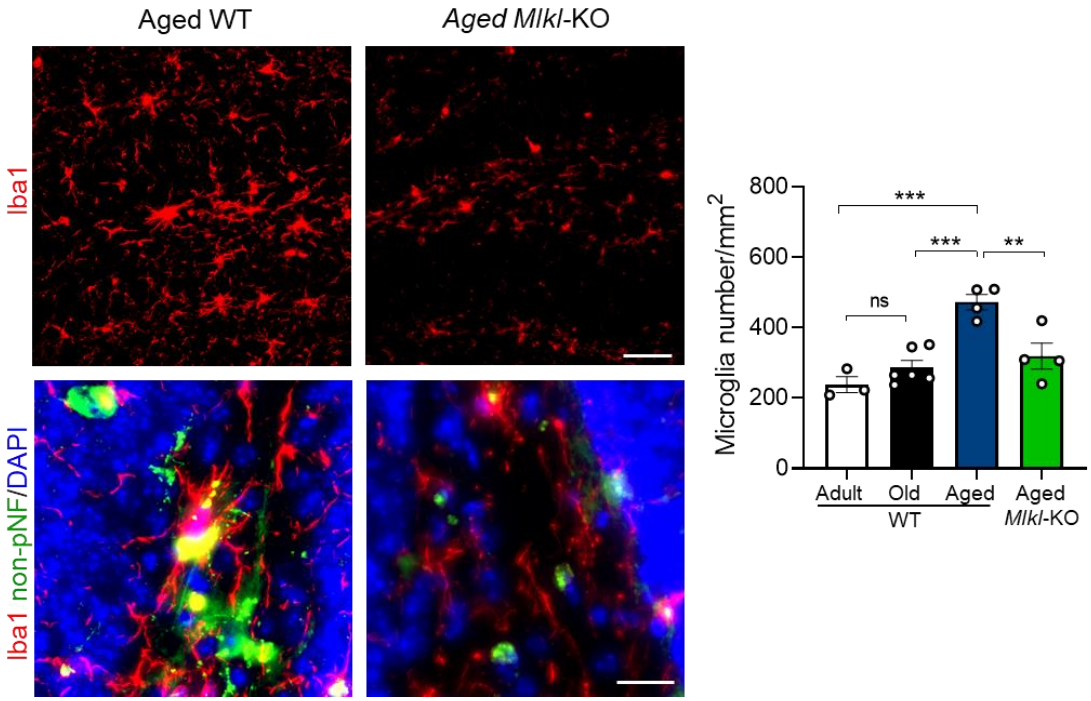

Fig S7. Age-dependent microgliosis is prevented by *Mlkl* loss. Microglia number was measured by Iba1 immunodetection and quantified as number of positive Iba1 cells in the hilus of the hippocampal DG and normalized to area (mm^2), (calibration bar, 50 µm). Microglia overlapping with degenerating axons were identify as Iba1+/non-pNF+ staining (yellow) in the hippocampus of aged mice (calibration bar, 20 µm). Values are the result of the analysis of n=3-5 mice per group. One-way ANOVA with Tukey analysis for multiple comparisons, **p<0.01, ***p<0.005.

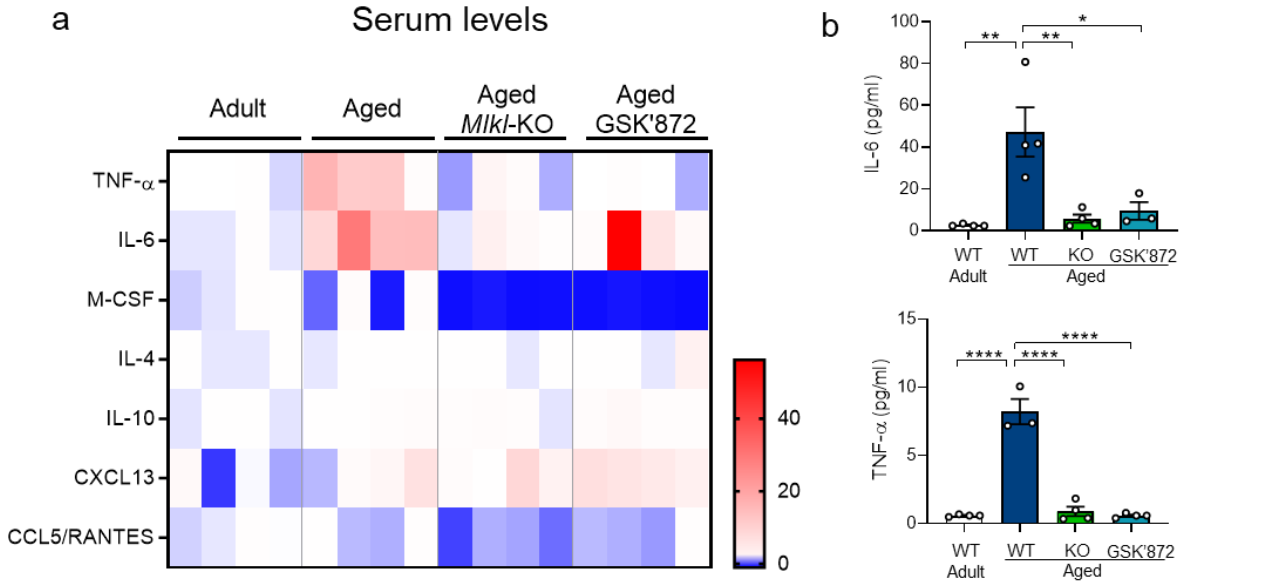

Fig S8. Systemic decrease of pro-inflammatory cytokines in aged mice with inhibited necroptosis. Cytokines levels in serum from adult versus aged WT and *Mlkl*-KO mice were assessed by Luminex High Performance Assay. **(a)** The heatmap shows fold change levels of cytokines and chemokines analyzed in the serum of adult versus aged, aged-*Mlkl*-KO and aged-GSK'872 treated mice (n=4, separated in each column). **(b)** Plots represent absolute cytokine levels (pg/ml) for IL-6 and TNF-α in serum samples of different mice groups. Error bars, mean ± SEM, *p:<0.05; **p<0.01; ****p<0.001. Statistical significance was determined by one-way ANOVA with Tukey analysis for multiple comparisons. One of the values corresponding to IL-6 levels in a GSK'872 mouse was considered outlier and excluded from the analysis. Outliers were identified with the "Identify Outliers" tool from GraphPad Prism v8.0.2.

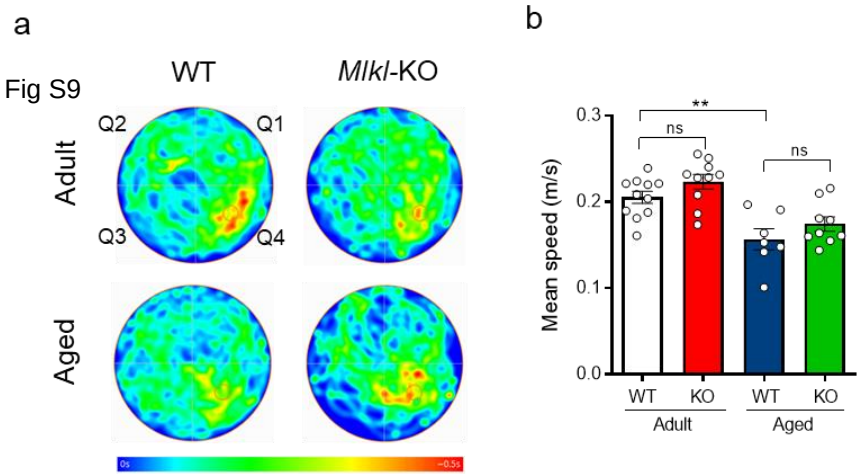

Fig S9. (a) Average heatmaps specify in pseudo-color the location of each mice cohort along time during memory testing (day 5). The quadrant Q4 designates the initial location of the hidden platform during training. **(b)** Mean swimming speed of mice during day 5 trial. Values are the result of the analysis of n=7-10 mice per group. One-way ANOVA with Tukey correction for multiple comparison, **p:<0.05.

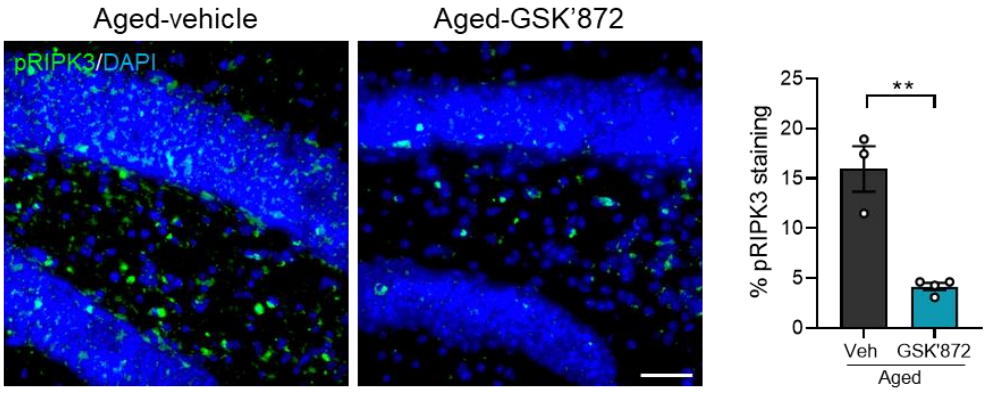

Fig S10. Decreased pRIPK3 in the hippocampus of aged mice treated with GSK´872. Efficiency of systemic treatment with the RIPK3 inhibitor and its impact in the brain was evaluated by detecting RIPK3 phosphorylation in the hippocampus of aged mice treated with GSK'872 (calibration bar, 50 µm). RIPK3 activation was measured as the percentage of pRIPK3 stained area. Error bars, mean ± SEM from n=3-4 mice. Statistical significance was determined by T-test with p=0.0018.

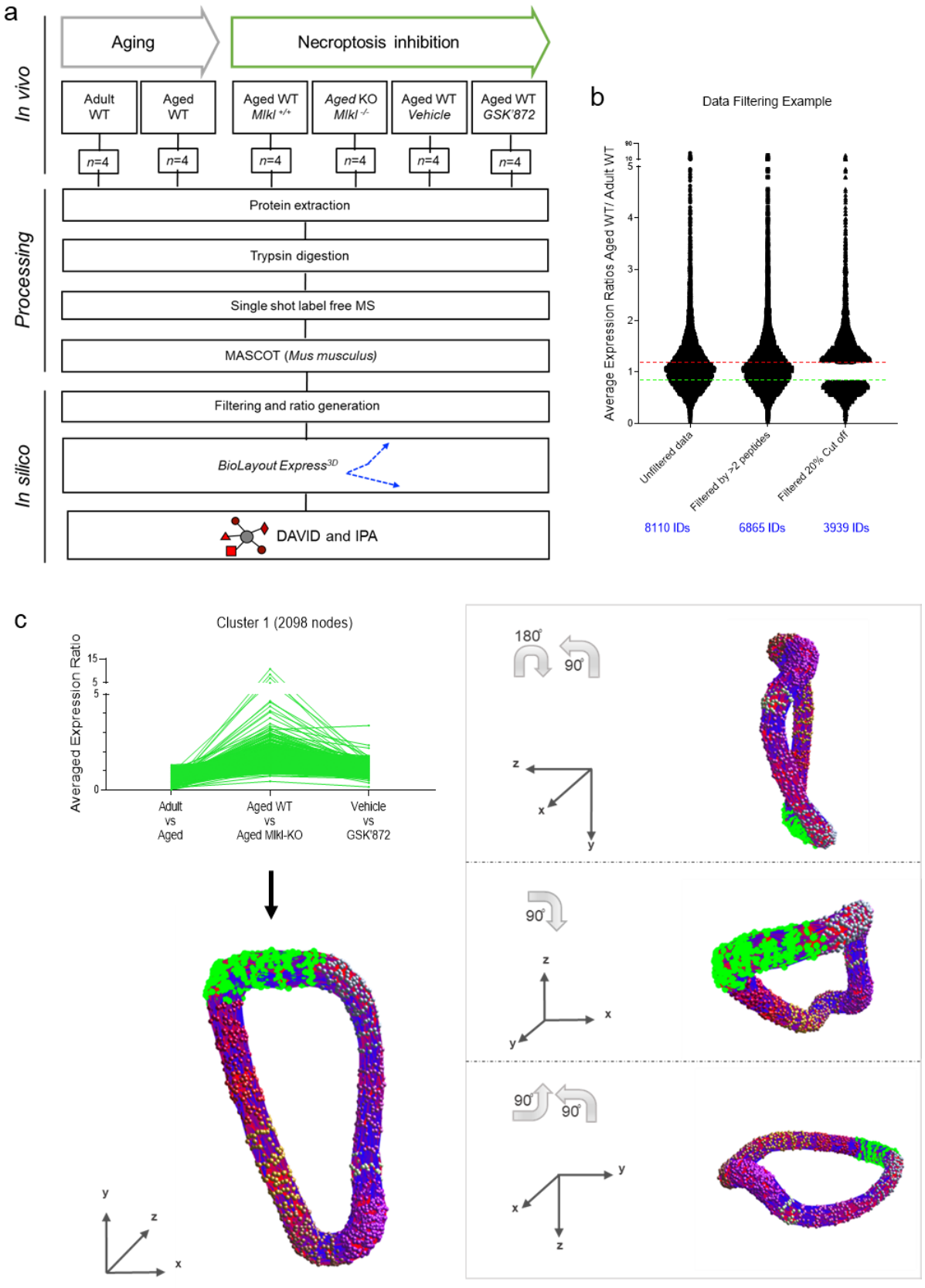
a
In vivo
Aging
Necroptosis inhibition
Adult WT
Aged WT
Aged WT Mlkl +/+
Aged KO Mlkl -/-
Aged WT Vehicle
Aged WT GSK'872
n=4
Processing
Protein extraction
Trypsin digestion
Single shot label free MS
MASCOT (Mus musculus)
In silico
Filtering and ratio generation
BioLayout Express3D
DAVID and IPA
b
Data Filtering Example
Average Expression Ratios Aged WT/ Adult WT
Unfiltered data
Filtered by >2 peptides
Filtered 20% Cut off
8110 IDs
6865 IDs
3939 IDs
c
Cluster 1 (2098 nodes)
Averaged Expression Ratio
Adult vs Aged
Aged WT vs Aged Mlkl-KO
Vehicle vs GSK'872
180°
90°

Fig S11. Proteomic sample processing and data analysis. (a) Workflow of proteomic analysis and processing of data. **(b)** Data filtering. Proteins identified by ≥ 2 unique peptides and ± 20% of changes were considered for subsequent analysis. **(c)** BioLayout expression analysis allows a 3D representation of the molecular changes between normal aging and necroptosis-targeted aging process. Each sphere represents an individual protein. Clusters (groupings of proteins delineated by color) can be further analyzed with other in silico tools such as DAVID thereby allowing the data to be broken down into more manageable groupings. Cluster 1 is shown in green as clustering example.

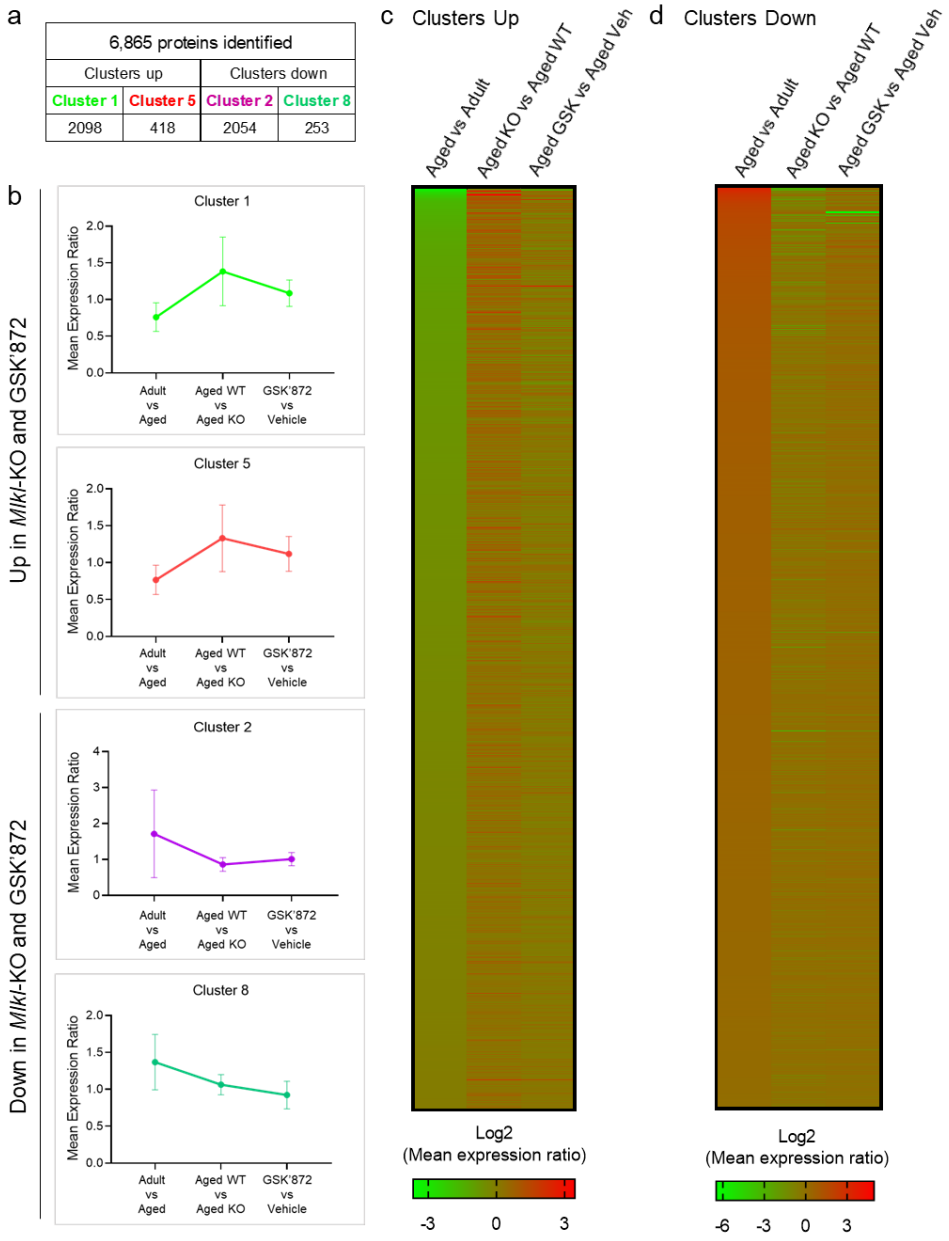

Fig S12. Proteomic data clustering and analysis. (a) Table containing information regarding the total number of proteins identified, and those belonging to each cluster of grouping proteins classified as "up" or "down" clusters. **(b)** Classification of clusters "up" and "down" was determined considering the mean expression ratio values and grouped according to their trend to be up- or down-regulated respectively in the genetic (aged *Mlkl*-ko vs aged WT) and pharmacologic (aged-GSK'872 vs aged-vehicle) model of necroptosis inhibition compared with normal aging (adult vs aged). **(c)** Heat maps illustrating the proteomic profile of each cluster show opposing directionality in expression between normal aging and necroptosis-inhibited processes in aged mice. Changes are expressed as log2 of the mean expression ratio.

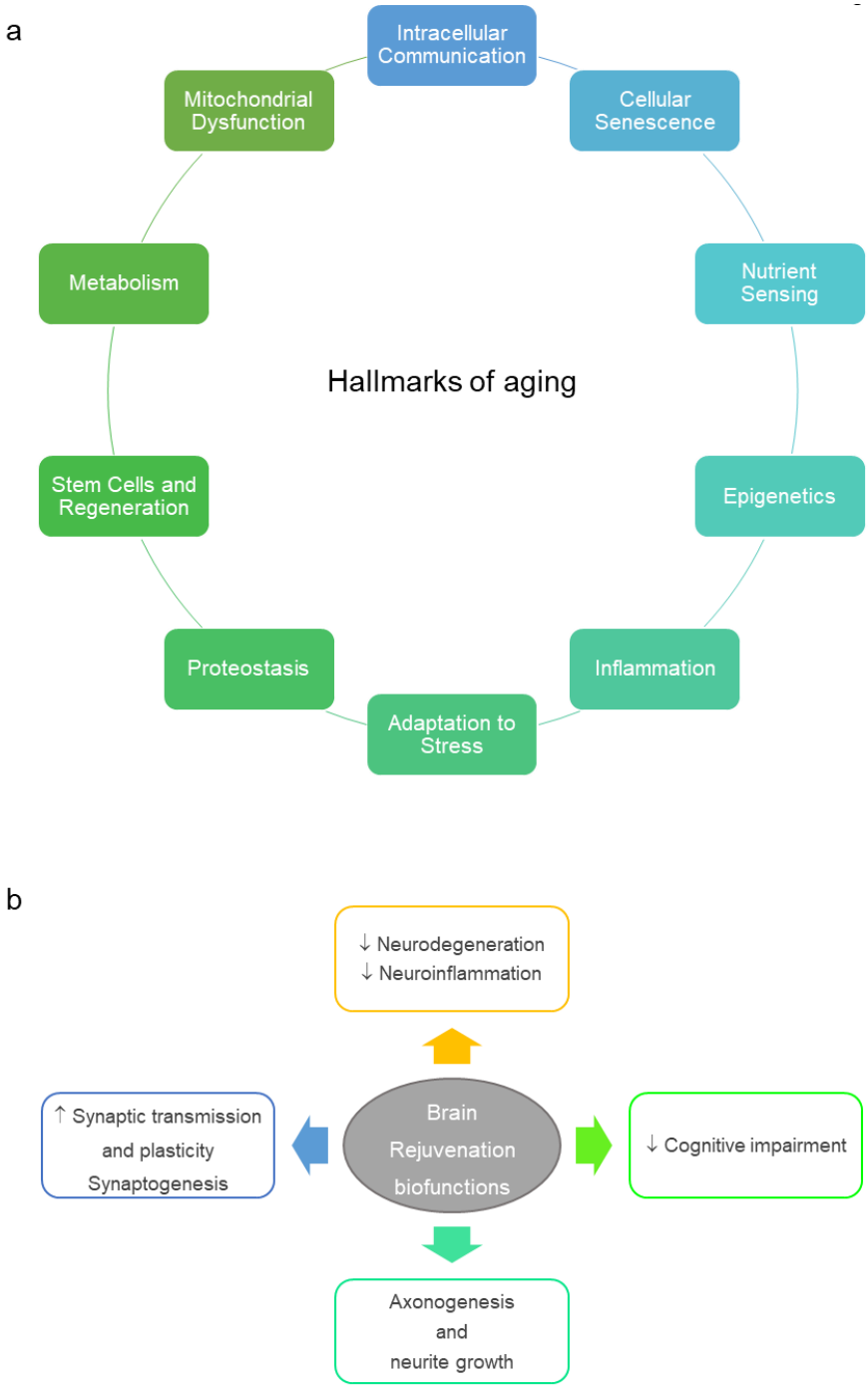

Fig S13. Pillars of aging and brain rejuvenation hallmarks modulated in the genetic and pharmacologic models of necroptosis inhibition.

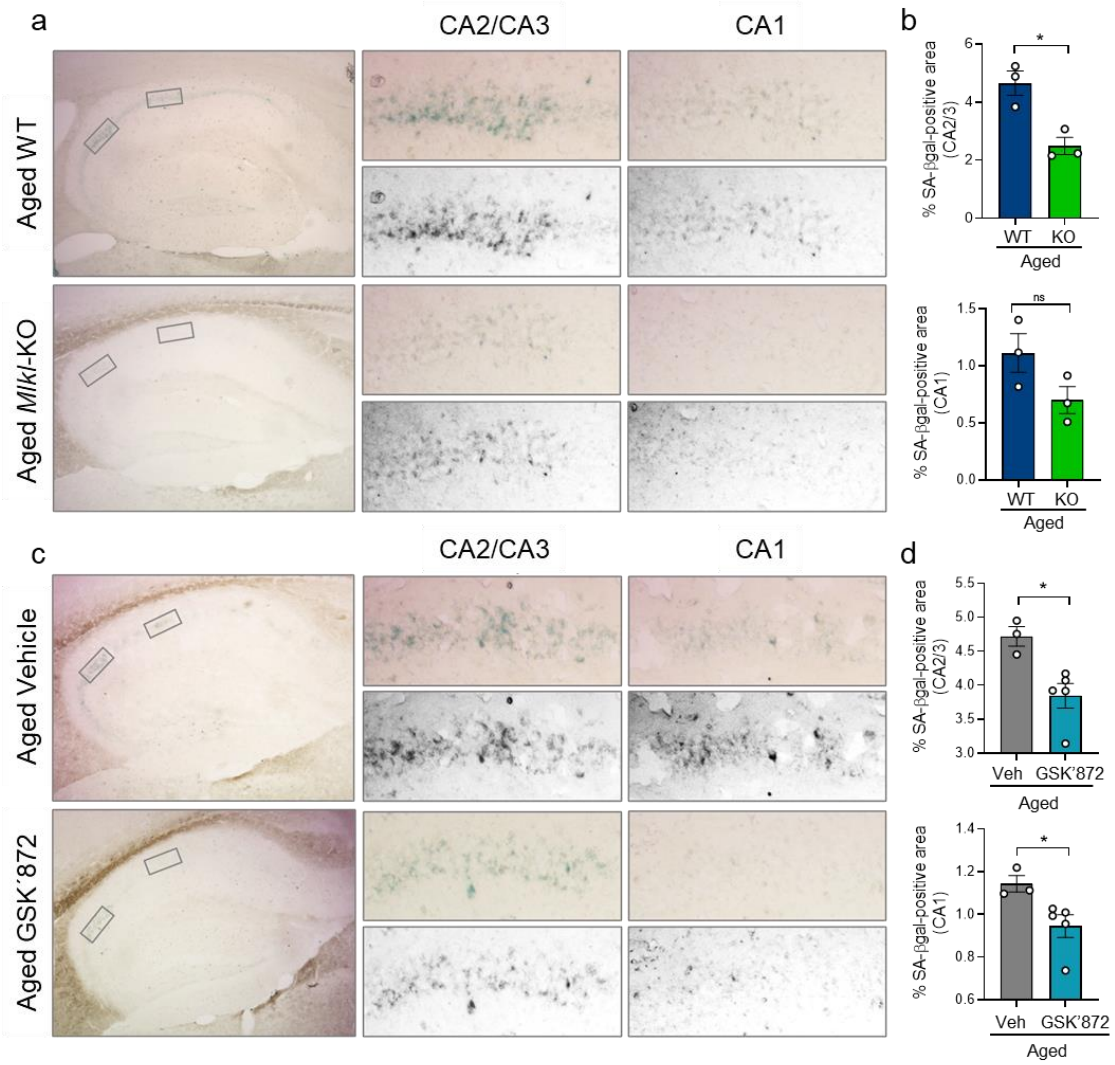

Fig S14. SA-*β*galactosidase activity in the CA1 and CA2/CA3 subfields of the hippocampus in aged mice treated with GSK'872. (a,b) SA-*β*galactosidase (SA-*β*gal) activity quantified in the hippocampus of aged WT vs aged *Mlkl*-KO mice. Magnifications of CA1 and CA2/3 areas show SA-*β*gal staining in grayscale. Quantification shows the percentage of the SA-*β*gal-positive area. **(c, d)** SA-*β*gal activity in the hippocampus of aged vehicle vs GSK'872-treated mice. Values, mean ± SEM (n=3-5). Unpaired T-test Student, *p<0.05.

a

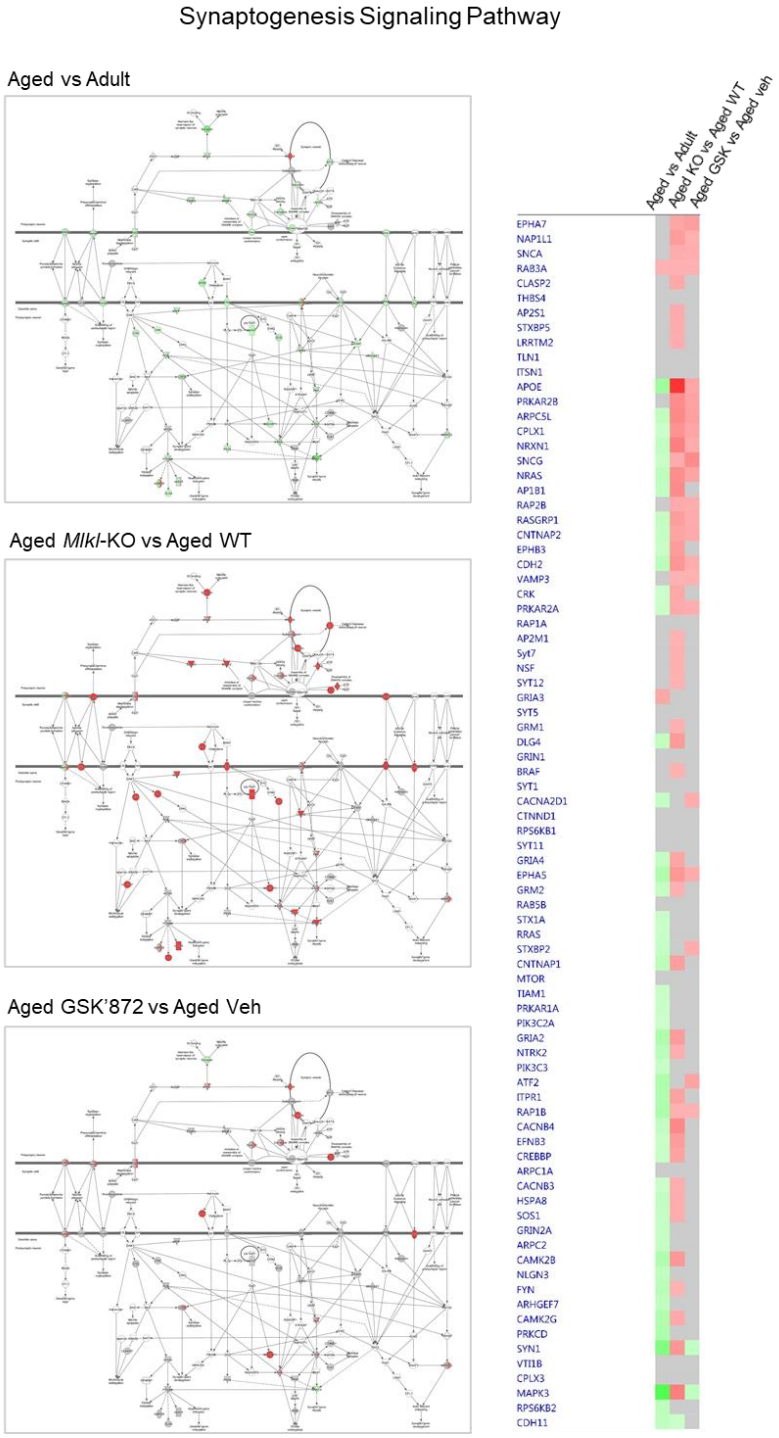

b

Synaptogenesis Pathway	Aged vs Adult	Aged Mlkl-KO vs Aged WT	Aged GSK'872 vs Aged Vehicle
Z-score	-5.98	5.98	3.273
p-value	1.82E-10	5.72E-11	1.63E-05

Fig S15. Schematic illustrating the canonical pathway annotation of "Synaptogenesis signaling pathway". **(a)** Top canonical pathway annotations were defined by ranking of absolute z-score between "normal" aging, *Mlkl*-KO and GSK'872 analyses. Intensity of colour represents magnitude of change; red corresponds to upregulation compared to control within each respective analysis, while green represents downregulation. Molecules in grey were identified to be necroptosis-correlative alterations present within input dataset, but fell below the 20% cut-off, while molecules in white were not present within input dataset but changed less than 20% in analysis. Solid connecting lines represent a direct interaction, while dashed connecting lines indicate an indirect interaction. Heat map of individual proteins assigned to the canonical pathway "*Synaptogenesis signaling*". Changes between normal aging and *Mlkl*-KO or GSK'872 treated mice were expressed as fold change. **(b)** Table shows statistical summaries from IPA for the Synaptogenesis cascade, including Z-score and p-value for each ratio.

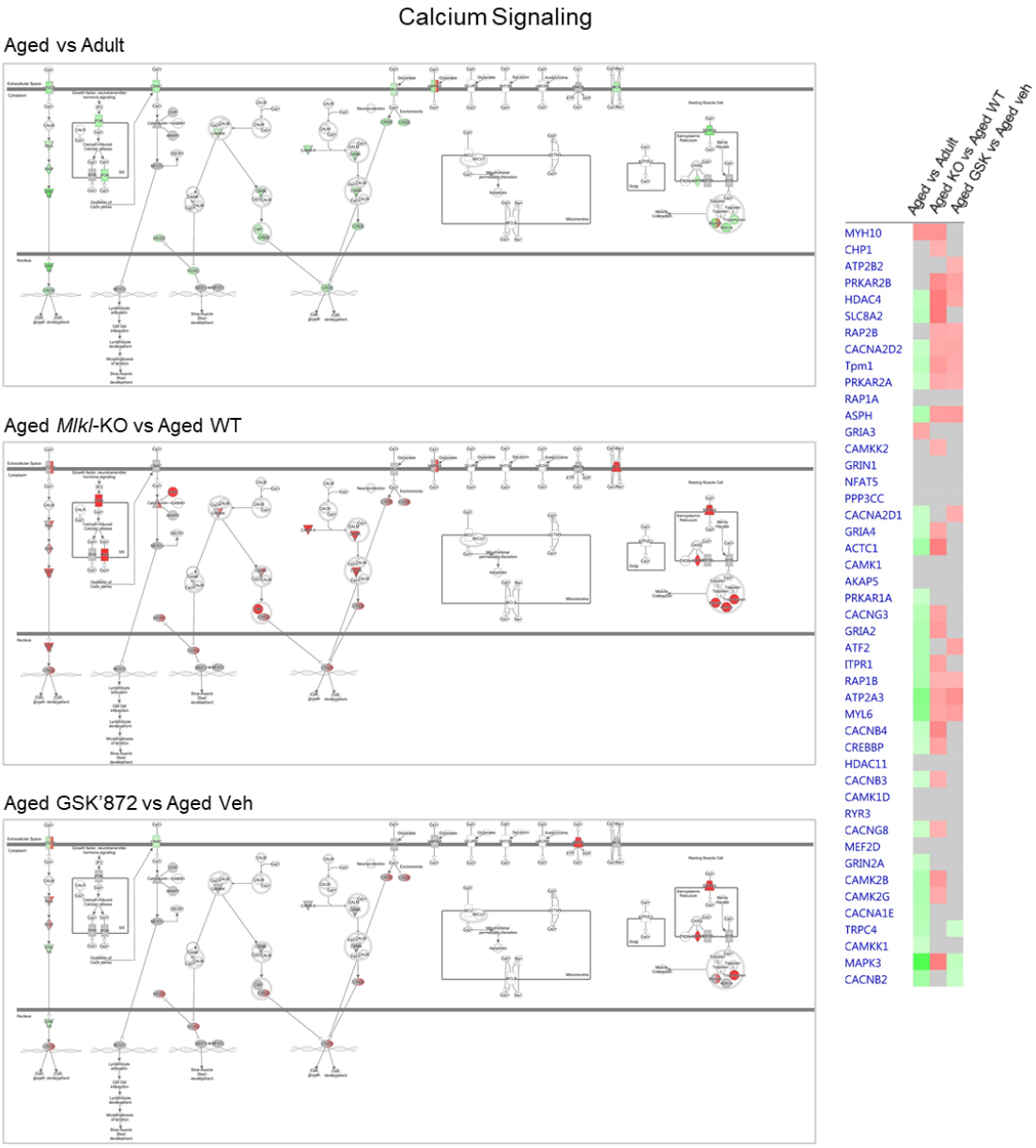

Fig S16. Schematic illustrating the canonical pathway annotation of "Calcium signaling". (a) Top canonical pathway annotations were defined by ranking of absolute z-score between "normal" aging, *Mlkl*-KO and GSK'872 analyses. Intensity of colour represents magnitude of change; red corresponds to upregulation compared to control within each respective analysis, while green represents downregulation. Molecules in grey were identified to be necroptosis-correlative alterations present within input dataset, but fell below the 20% cut-off, while molecules in white were not present within input dataset. Solid connecting lines represent a direct interaction, while dashed connecting lines indicate an indirect interaction. Heat map of individual proteins assigned to the canonical pathway "*Calcium signaling*". Changes between normal aging and *Mlkl*-KO or GSK'872 treated mice were expressed as fold change.

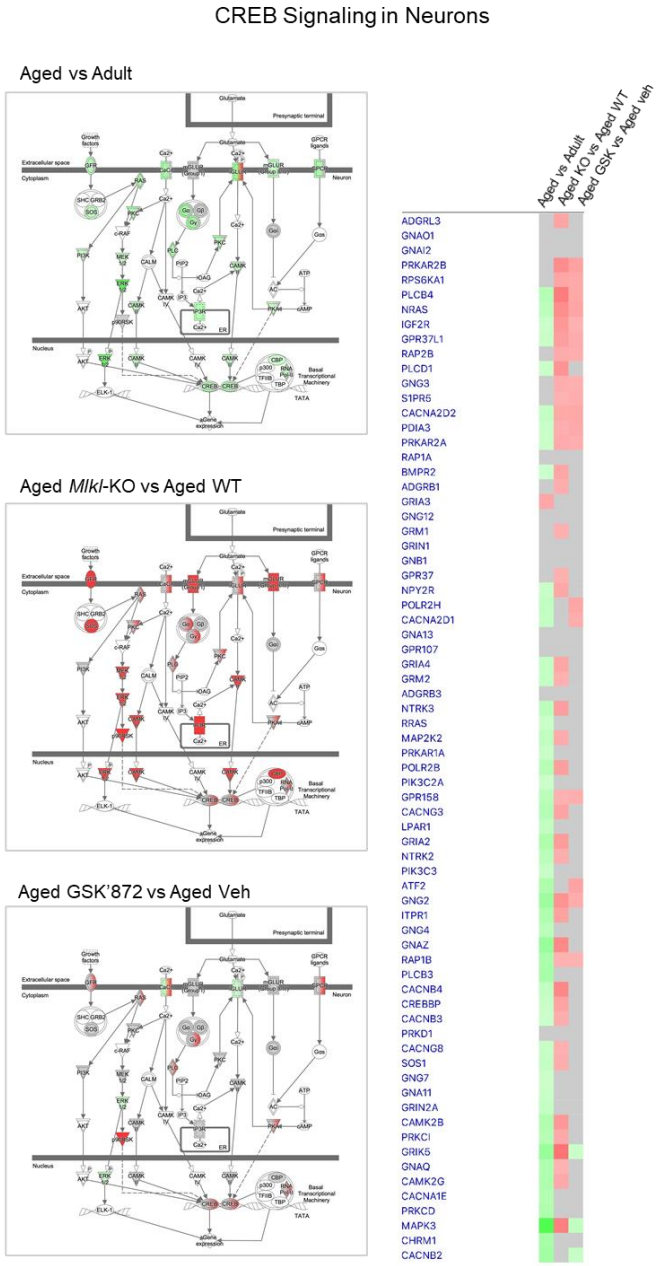

Fig S17. Schematic illustrating the canonical pathway annotation of "CREB signaling in neurons". (a) Top canonical pathway annotations were defined by ranking of absolute z-score between "normal" aging, *Mlkl*-KO and GSK'872 analyses. Intensity of colour represents magnitude of change; red corresponds to upregulation compared to control within each respective analysis, while green represents downregulation. Molecules in grey were identified to be necroptosis-correlative alterations present within input dataset, but fell below the 20% cut-off, while molecules in white were not present within input dataset. Solid connecting lines represent a direct interaction, while dashed connecting lines indicate an indirect interaction. Heat map of individual proteins assigned to the canonical pathway "*CREB signaling in neurons*". Changes between normal aging and *Mlkl*-KO or GSK'872 treated mice were expressed as fold change.

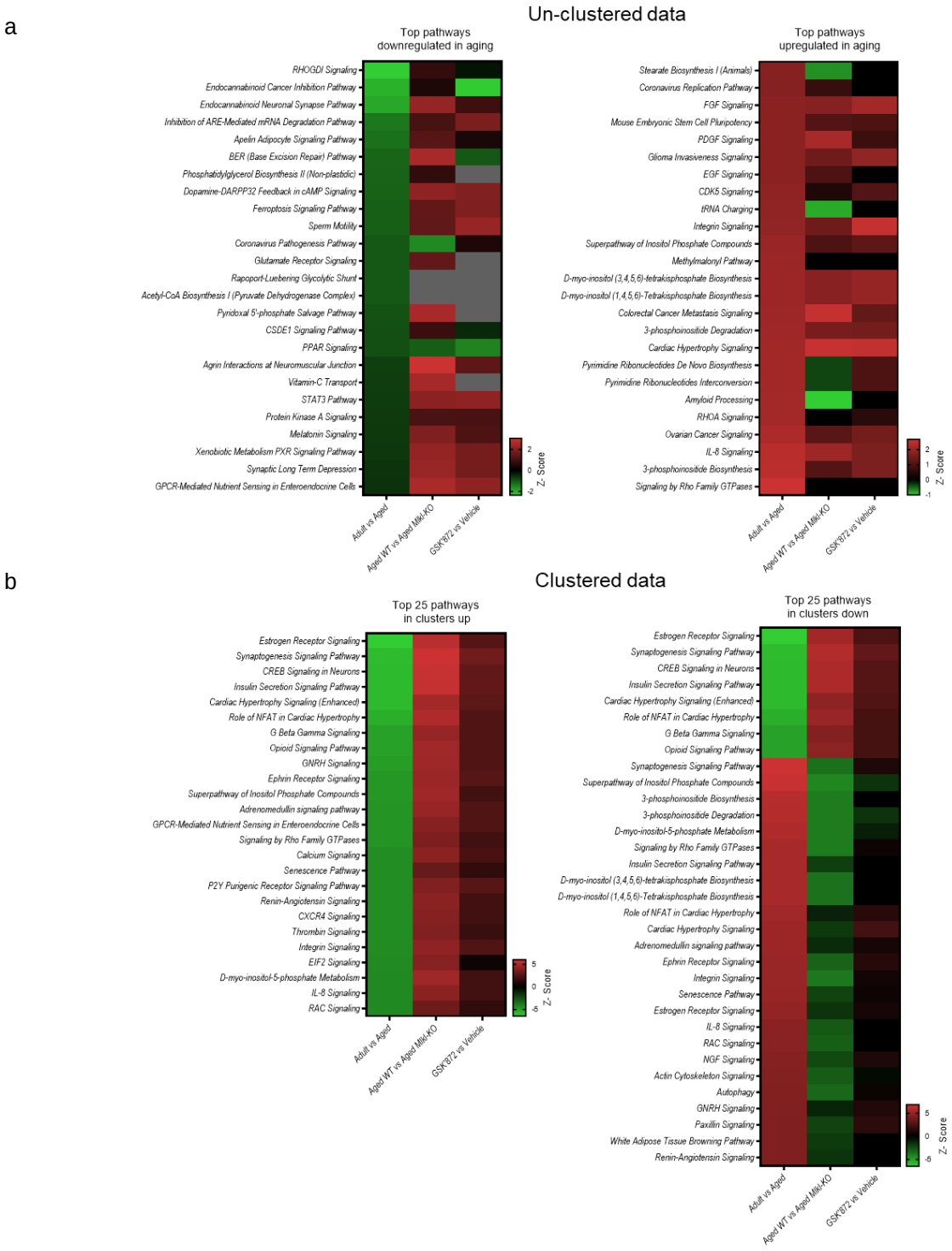

Fig S18. Top 25 pathways modulated by necroptosis inhibition. (a) Heat maps illustrating the proteomic profile of the un-clustered data (predicted z-score) of the top pathways up and downregulated in aging. **(b)** Heat maps representing the proteomic profile of the top pathways modulated in the up and down clusters show opposing directionality in expression between normal aging and necroptosis-inhibited processes in aged mice.

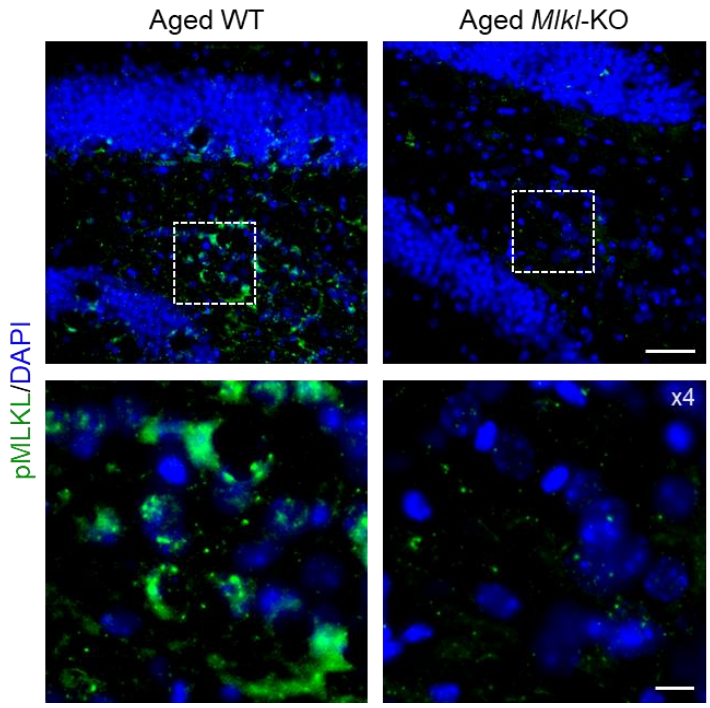

Fig S19. Phospho-MLKL antibody validation in aged Mlkl-KO mice. The commercial pMLKL antibody (phospho S345, Abcam, ab196436) was used as a readout of necroptosis activation in hippocampal tissue of aged mice. The pMLKL signal (green) observed in aged mice was validated in the *Mlkl*-KO mouse model by the absence of labeling (calibration bar, 50 µm). White dotted boxes define amplified images at the bottom (x4), showing the staining pattern of pMLKL in the hilus of the hippocampus of aged mice (calibration bar, 10 µm).

Table S1. Information of analytes evaluated by Luminex High Performance Assay.

ANALYTE	BEAD REGION	STANDARD CURVE (pg/ml)	SENSITIVITY (pg/ml)	MAIN FUNCTIONS	REFERENCES
CCL2/JE/MCP-1	18	221 - 53,720	134	Chemokine, regulates migration and infiltration of monocytes/macrophages.	(Barna et al. 1994; Deshmane et al. 2009)
CCL5/RANTES	38	88.9 - 21,610	19.1	Chemokine, drives mononuclear cells migration across the blood brain barrier (BBB).	(Ubogu et al. 2006; Lanfranco et al. 2018)
CXCL13/BLC/BCA-1	21	187 - 45,530	19.3	Chemokine, B and T lymphocytes chemoattractant.	(Irani 2016; Pilz et al. 2020)
IFN-gamma	33	12.3 - 2,990	1.85	Pro-inflammatory cytokine, microglia priming, regulates immune response genes.	(Roy et al. 2020; Monteiro et al. 2015)
IL-1 beta/IL-1F2	19	221 - 53,780	41.8	Pro-inflammatory cytokine, induces expression of TNF-α and IL-6 to promote neuroinflammation.	(Basu et al. 2004; Shaftel et al. 2008)
IL-2	22	7.7 - 1,860	0.481	Anti-inflammatory cytokine, regulatory T cells function and survival in autoimmune and inflammatory diseases.	(Ross & Cantrell 2018; Klatzmann & Abbas 2015)
IL-4	25	56.4 - 13,700	53	Anti-inflammatory cytokine, inhibits IL-1, IL-6 and TNF-α production. Neuroprotective effects.	(Te Velde et al. 1990; Di Benedetto et al. 2017)
IL-6	27	24.6 - 5,970	2.3	Pro-inflammatory cytokine, induces microglia activation and BBB permeability. Senescence marker.	(Jurk et al. 2012; Erta et al. 2012)
IL-10	28	11.7 - 2,840	8.2	Anti-inflammatory cytokine, inhibits IL-1, IL-12 and TNF-α production.	(O'Garra & Vieira 2007; Lobo-Silva et al. 2016)
IL-12 p70	15	42.1 - 10,240	12.8	Pro-inflammatory cytokine required for IFN-γ and TNF-α production. Produces in the brain by microglia.	(Trinchieri 2003; Hofer et al. 2004)
M-CSF	45	1.85 - 450	0.404	Cytokine, regulates proliferation of macrophages. Microglia polarization towards M1/M2 phenotype.	(Hamilton et al. 2014; Pons & Rivest 2018)
TNF-alpha	14	3.2 - 790	1.47	The main pro-inflammatory cytokine, activates cell death cascades. Critical for immunoinflammatory response.	(Duque & Descoteaux 2014; Horiuchi et al. 2010)

Table S2. Inclusion list. Mass spectrometry isolation windows for data independent acquisition analysis. Refer to the corresponding method details section for further information.

Window	Start m/z	End m/z	Width	Centre	Window	Start m/z	End m/z	Width	Centre
1	349.5	376.5	27	363	**36**	642.5	650.5	8	646.5
2	375.5	396.5	21	386	**37**	649.5	657.5	8	653.5
3	395.5	410.5	15	403	**38**	656.5	664.5	8	660.5
4	409.5	424.5	15	417	**39**	663.5	671.5	8	667.5
5	423.5	435.5	12	429.5	**40**	670.5	678.5	8	674.5
6	434.5	445.5	11	440	**41**	677.5	685.5	8	681.5
7	444.5	454.5	10	449.5	**42**	684.5	692.5	8	688.5
8	453.5	461.5	8	457.5	**43**	691.5	700.5	9	696
9	460.5	468.5	8	464.5	**44**	699.5	709.5	10	704.5
10	467.5	475.5	8	471.5	**45**	708.5	718.5	10	713.5
11	474.5	482.5	8	478.5	**46**	717.5	726.5	9	722
12	481.5	489.5	8	485.5	**47**	725.5	734.5	9	730
13	488.5	495.5	7	492	**48**	733.5	743.5	10	738.5
14	494.5	502.5	8	498.5	**49**	742.5	752.5	10	747.5
15	501.5	509.5	8	505.5	**50**	751.5	760.5	9	756
16	508.5	516.5	8	512.5	**51**	759.5	770.5	11	765
17	515.5	522.5	7	519	**52**	769.5	780.5	11	775
18	521.5	529.5	8	525.5	**53**	779.5	790.5	11	785
19	528.5	536.5	8	532.5	**54**	789.5	801.5	12	795.5
20	535.5	543.5	8	539.5	**55**	800.5	812.5	12	806.5
21	542.5	549.5	7	546	**56**	811.5	826.5	15	819
22	548.5	555.5	7	552	**57**	825.5	839.5	14	832.5
23	554.5	561.5	7	558	**58**	838.5	852.5	14	845.5
24	560.5	567.5	7	564	**59**	851.5	866.5	15	859
25	566.5	573.5	7	570	**60**	865.5	880.5	15	873
26	572.5	580.5	8	576.5	**61**	879.5	896.5	17	888
27	579.5	587.5	8	583.5	**62**	895.5	916.5	21	906
28	586.5	594.5	8	590.5	**63**	915.5	936.5	21	926
29	593.5	602.5	9	598	**64**	935.5	958.5	23	947
30	601.5	609.5	8	605.5	**65**	957.5	980.5	23	969
31	608.5	615.5	7	612	**66**	979.5	1010.5	31	995
32	614.5	622.5	8	618.5	**67**	1009.5	1042.5	33	1026
33	621.5	629.5	8	625.5	**68**	1041.5	1085.5	44	1063.5
34	628.5	636.5	8	632.5	**69**	1084.5	1150.5	66	1117.5
35	635.5	643.5	8	639.5					

SUPPLEMENTARY REFERENCES

Barna BP, Pettay J, Barnett GH, Zhou P, Iwasaki K & Estes ML (1994) Regulation of monocyte chemoattractant protein-1 expression in adult human non-neoplastic astrocytes is sensitive to tumor necrosis factor (TNF) or antibody to the 55-kDa TNF receptor. *J. Neuroimmunol.* 50, 101–107. Available at: https://pubmed.ncbi.nlm.nih.gov/8300851/ [Accessed May 5, 2021].

Basu A, Krady JK & Levison SW (2004) Interleukin-1: A master regulator of neuroinflammation. *J. Neurosci. Res.* 78, 151–156. Available at: https://pubmed.ncbi.nlm.nih.gov/15378607/ [Accessed May 7, 2021].

Di Benedetto S, Müller L, Wenger E, Düzel S & Pawelec G (2017) Contribution of neuroinflammation and immunity to brain aging and the mitigating effects of physical and cognitive interventions. *Neurosci. Biobehav. Rev.* 75, 114–128. Available at: http://dx.doi.org/10.1016/j.neubiorev.2017.01.044.

Deshmane SL, Kremlev S, Amini S & Sawaya BE (2009) Monocyte chemoattractant protein-1 (MCP-1): An overview. *J. Interf. Cytokine Res.* 29, 313–325. Available at: /pmc/articles/PMC2755091/ [Accessed May 5, 2021].

Duque GA & Descoteaux A (2014) Macrophage cytokines: Involvement in immunity and infectious diseases. *Front. Immunol.* 5. Available at: /pmc/articles/PMC4188125/ [Accessed May 26, 2021].

Erta M, Quintana A & Hidalgo J (2012) Interleukin-6, a major cytokine in the central nervous system. *Int. J. Biol. Sci.* 8, 1254–1266.

Hamilton TA, Zhao C, Pavicic PG & Datta S (2014) Myeloid colony-stimulating factors as regulators of macrophage polarization. *Front. Immunol.* 5, 1–6.

Hofer M, Hausmann J, Staeheli P & Pagenstecher A (2004) Cerebral expression of interleukin-12 induces neurological disease via differential pathways and recruits antigen-specific T cells in virus-infected mice. *Am. J. Pathol.* 165, 949–958. Available at: /pmc/articles/PMC1618590/ [Accessed May 14, 2021].

Horiuchi T, Mitoma H, Harashima SI, Tsukamoto H & Shimoda T (2010) Transmembrane TNF-α: Structure, function and interaction with anti-TNF agents. *Rheumatology* 49, 1215–1228. Available at: https://academic.oup.com/rheumatology/article/49/7/1215/1785515 [Accessed May 26, 2021].

Irani DN (2016) Regulated Production of CXCL13 within the Central Nervous System. *J. Clin. Cell. Immunol.* 7. Available at: /pmc/articles/PMC5461933/ [Accessed May 7, 2021].

Jurk D, Wang C, Miwa S, Maddick M, Korolchuk V, Tsolou A, Gonos ES, Thrasivoulou C, Jill Saffrey M, Cameron K & von Zglinicki T (2012) Postmitotic neurons develop a p21-dependent senescence-like phenotype driven by a DNA damage response. *Aging Cell* 11, 996–1004.

Klatzmann D & Abbas AK (2015) The promise of low-dose interleukin-2 therapy for autoimmune and inflammatory diseases. *Nat. Rev. Immunol.* 15, 283–294.

Lanfranco MF, Mocchetti I, Burns MP & Villapol S (2018) Glial- and neuronal-specific expression of CCL5 mRNA in the rat brain. *Front. Neuroanat.* 11. Available at: /pmc/articles/PMC5770405/ [Accessed May 5, 2021].

Lobo-Silva D, Carriche GM, Castro AG, Roque S & Saraiva M (2016) Balancing the immune response in the brain: IL-10 and its regulation. *J. Neuroinflammation* 13, 1–10. Available at: https://jneuroinflammation.biomedcentral.com/articles/10.1186/s12974-016-0763-8 [Accessed March 24, 2021].

Monteiro S, Ferreira FM, Pinto V, Roque S, Morais M, De Sá-Calcąda D, Mota C, Correia-Neves M & Cerqueira JJ (2015) Absence of IFNγ promotes hippocampal plasticity and enhances cognitive performance. *Transl. Psychiatry* 5, 707. Available at: www.nature.com/tp [Accessed May 7, 2021].

Murphy JM, Czabotar PE, Hildebrand JM, Lucet IS, Zhang JG, Alvarez-Diaz S, Lewis R, Lalaoui N, Metcalf D, Webb AI, Young SN, Varghese LN, Tannahill GM, Hatchell EC, Majewski IJ, Okamoto T, Dobson RCJ, Hilton DJ, Babon JJ, Nicola NA, Strasser A, Silke J & Alexander WS (2013) The pseudokinase MLKL mediates necroptosis via a molecular switch mechanism. *Immunity* 39, 443–453. Available at:

http://dx.doi.org/10.1016/j.immuni.2013.06.018.

O'Garra A & Vieira P (2007) TH1 cells control themselves by producing interleukin-10. *Nat. Rev. Immunol.* 7, 425–428. Available at: https://pubmed.ncbi.nlm.nih.gov/17525751/ [Accessed May 12, 2021].

Pilz G, Sakic I, Wipfler P, Kraus J, Haschke-Becher E, Hitzl W, Trinka E & Harrer A (2020) Chemokine CXCL13 in serum, CSF and blood-CSF barrier function: Evidence of compartment restriction. *Fluids Barriers CNS* 17, 7. Available at: https://doi.org/10.1186/s12987-020-0170-5 [Accessed May 7, 2021].

Pons V & Rivest S (2018) New therapeutic avenues of mCSF for brain diseases and injuries. *Front. Cell. Neurosci.* 12, 1–6.

Ross SH & Cantrell DA (2018) Signaling and Function of Interleukin-2 in T Lymphocytes. *Annu. Rev. Immunol.* 36, 411–433. Available at: /pmc/articles/PMC6472684/ [Accessed May 12, 2021].

Roy ER, Wang B, Wan YW, Chiu G, Cole A, Yin Z, Propson NE, Xu Y, Jankowsky JL, Liu Z, Lee VMY, Trojanowski JQ, Ginsberg SD, Butovsky O, Zheng H & Cao W (2020) Type I interferon response drives neuroinflammation and synapse loss in Alzheimer disease. *J. Clin. Invest.* 130, 1912–1930. Available at: https://doi.org/10.1172/JCI133737DS1 [Accessed May 7, 2021].

Shaftel SS, Griffin WST & Kerry KM (2008) The role of interleukin-1 in neuroinflammation and Alzheimer disease: An evolving perspective. *J. Neuroinflammation* 5, 7. Available at: /pmc/articles/PMC2335091/ [Accessed May 7, 2021].

Trinchieri G (2003) Interleukin-12 and the regulation of innate resistance and adaptive immunity. *Nat. Rev. Immunol.* 3, 133–146.

Ubogu EE, Callahan MK, Tucky BH & Ransohoff RM (2006) Determinants of CCL5-driven mononuclear cell migration across the blood-brain barrier. Implications for therapeutically modulating neuroinflammation. *J. Neuroimmunol.* 179, 132–144. Available at: https://pubmed.ncbi.nlm.nih.gov/16857269/ [Accessed May 5, 2021].

Te Velde AA, Huijbens RJF, Heije K, De Vries JE & Figdor CG (1990) Interleukin-4 (IL-4) inhibits secretion of IL-1β, tumor necrosis factor α, and IL-6 by human monocytes. *Blood* 76, 1392–1397.